

HST Observations of the Double-Peaked Emission Lines in the Seyfert Galaxy Markarian 78: Mass Outflows from a Single AGN¹

T.C. Fischer², D.M. Crenshaw², S.B. Kraemer³, H.R. Schmitt⁴, R.F. Mushotsky⁵, J.P. Dunn⁶

ABSTRACT

Previous ground based observations of the Seyfert 2 galaxy Mrk 78 revealed a double set of emission lines, similar to those seen in several active galactic nuclei (AGN) from recent surveys. Are the double lines due to two AGN with different radial velocities in the same galaxy, or are they due to mass outflows from a single AGN? We present a study of the outflowing ionized gas in the resolved narrow-line region (NLR) of Mrk 78 using observations from Space Telescope Imaging Spectrograph (STIS) and Faint Object Camera (FOC) aboard the *Hubble Space Telescope* (HST) as part of an ongoing project to determine the kinematics and geometries of AGN outflows. From the spectroscopic information, we determined the fundamental geometry of the outflow via our kinematics modeling program by recreating radial velocities to fit those seen in four different STIS slit positions. We determined that the double emission lines seen in ground-based spectra are due to an asymmetric distribution of outflowing gas in the NLR. By successfully fitting a model for a single AGN to Mrk 78, we show that it is possible to explain double emission lines with radial velocity offsets seen in AGN similar to Mrk 78 without requiring dual supermassive black holes.

¹Based on observations made with the NASA/ESA Hubble Space Telescope, obtained at the Space Telescope Science Institute, which is operated by the Association of Universities for Research in Astronomy, Inc. under NASA contract NAS 5-26555.

²Department of Physics and Astronomy, Georgia State University, Astronomy Offices, One Park Place South SE, Suite 700, Atlanta, GA 30303; fischer@chara.gsu.edu

³Institute for Astrophysics and Computational Sciences, Department of Physics, The Catholic University of America, Washington, DC 20064

⁴Computational Physics, Inc, Springfield, VA 22151-2110; and Naval Research Laboratory, Washington, DC 20375

⁵Department of Astronomy, University of Maryland, College Park, MD 20742-2421

⁶Department of Chemistry and Physics, Augusta State University, Augusta, GA 30904

Subject headings: galaxies: Seyfert – galaxies: individual (Mrk 78)

1. Introduction

Narrow line regions of Seyfert galaxies contain photoionized gas due to the nonstellar continuum emitted by the AGN and are structured roughly in the shape of a bicone, where the apex of the bicone is located in the center of the AGN (Pogge 1988; Schmitt et al. 1994). This likely indicates that the ionizing radiation from the nucleus is being collimated by an absorbing material, which could be a torus-like structure (Antonucci 1993) or perhaps a disk wind (Elitzur & Shlosman 2006). However, the source of the NLR gas is not well understood.

An AGN of particular interest is Mrk 78. Classified as an SB galaxy in the NASA/IPAC Extragalactic Database (NED), it is also a Seyfert 2 galaxy because only narrow (full width at half-maximum [FWHM] $\leq 1000 \text{ km s}^{-1}$) emission lines are present in its optical spectra. With a redshift of $z = 0.036793$ based on Ca T stellar absorption lines (Nelson & Whittle 1995), Mrk 78 is at a distance of $\sim 150 \text{ Mpc}$ (for $H_0 = 73 \text{ km s}^{-1} \text{ Mpc}^{-1}$); at this distance, $1''$ corresponds to a transverse size of $\sim 730 \text{ pc}$. Mrk 78 has been extensively studied due to a visual correlation between the its radio source and extended narrow-line region (ENLR) (Whittle et al. 2002; Whittle & Wilson 2004; Whittle et al. 2005). *HST* FOC images of Mrk 78 in [O III] show that its narrow-line region (NLR) consists of two highly luminous regions extending over $\sim 5''$ ($\sim 3.6 \text{ kpc}$) that is in a biconical geometry also seen in several other Seyfert 2 galaxies (Schmitt et al. 2003). Thus, Mrk 78 makes for an interesting addition to our ongoing study to determine the geometries of the outflows and fueling flows in the NLRs of AGN (Das et al. 2005, 2006; Crenshaw et al. 2010a; Fischer et al. 2010).

A specifically interesting aspect is that ground-based spectroscopic observations of Mrk 78 have shown that its narrow emission lines are double peaked (Sargent 1972; Adams 1973). Ground-based spectra at high spectral resolution depict the [O III] emission-line profile as two large, well-defined peaks separated by $\sim 800 \text{ km s}^{-1}$ (Whittle et al. 1988; Nelson & Whittle 1995). As of late, there has been considerable activity around the study of double emission lines as they have been used as an indication for the presence of multiple AGN in a single galaxy. As such, Mrk 78 would seem an excellent candidate to test for multiple AGN as it is nearby, can be studied in detail, and contains dual-peaked lines with a velocity separation similar to those seen in other examples where "dual AGN" were decided a more likely scenario than outflows or rotating disks (Komossa et al. 2008; Comerford et al. 2009; Liu et al. 2010).

Crenshaw et al. (2010a) showed that velocity offsets between the narrow emission lines and host galaxy lines can be explained by the combination of mass outflows and dust extinction in AGN, or even an asymmetric distribution of outflowing gas. They also suggested that these explanations could possibly work for double-lined AGN, such as Mrk 78, as well. Previous studies had already suggested that radial motion via inflows or outflows could be responsible for the narrow line asymmetries and velocity shifts (Whittle 1985;

Dahari & De Robertis 1988; De Robertis & Shaw 1990), including long-slit ground-based observations that gave evidence for the production of asymmetries via outflows and dust obscuration (Storchi-Bergmann et al. 1992; Arribas et al. 1996; Christopoulou et al. 1997; Ramos Almeida et al. 2006; Rodríguez-Ardila et al. 2006). In this paper, we use high resolution spectroscopy and imaging to show that the velocity offset seen in Mrk 78 can indeed be explained by mass outflows in the NLR.

2. Observations

We obtained archival Space Telescope Imaging Spectrograph (STIS) long-slit spectra and Faint Object Camera (FOC) images of Mrk 78 from the Multimission Archive at the Space Telescope Science Institute (MAST). Four sets of spectra were taken between 1998 February 28 and 1998 March 01 under Hubble Program ID 7404 (M. Whittle, PI) with a $52'' \times 0''.2$ slit using a medium-dispersion G430M grating (4950 - 5240Å), which includes [O III] $\lambda 5007$. The spectral resolution was $0.56 \text{ Å} (\sim 30 \text{ km s}^{-1} \text{ FWHM})$, with an angular resolution of $0''.051$ per pixel in the cross dispersion direction. Of the four observations, three were taken at a position angle of 88° and the fourth was taken at a position angle of 61° . Additional details of each observation are given in Tables 1 and 2.

Figure 1 shows an extended continuum STIS acquisition image of Mrk 78 with additional, contoured [O III] and UV FOC images and positions for the four STIS slits illustrated on the [O III] image. The slits are offset from the optical continuum peak, signified as a "+", which was located by aligning the [O III] and continuum FOC images taken on the same date (Schmitt et al. 2003) and is also coincident with the infrared peak as observed by Ramos Almeida et al. (2006).

The STIS spectra were processed using IDL software developed at NASA's Goddard Space Flight Center for the STIS Instrument Definition Team. Cosmic-ray hits were removed before further processing. The zero point of the wavelength scales were corrected using wavelength-calibration exposures taken after each observation. Finally, the spectra were combined, geometrically rectified, and flux calibrated to provide spectral images that have a constant wavelength along each column and display fluxes in units of $\text{erg s}^{-1} \text{ cm}^{-2} \text{ Å}^{-1}$ per cross-dispersion pixel. The calibrated spectral images for each slit position can be found in Whittle et al. (2002).

We used the STIS spectra to compare our results with those taken from previous ground-based spectra, obtained through apertures that included most, if not all, of the NLR in Mrk 78 at moderate spectral resolution ($80\text{-}230 \text{ km s}^{-1} \text{ FWHM}$) (Vrtilek & Carleton 1985;

Nelson & Whittle 1995). The STIS datasets consist of hundreds of spectra along each slit, allowing us to resolve individual emission-line knots that are responsible for a majority of the emission seen in NLRs. To simulate the ground-based spectra, we combined all of the STIS spectra along each slit position and then combined the spectra from each slit, excluding slit D as it overlaps the other three slits, similar to the procedure in Crenshaw et al. (2010b). Figure 2 shows the final co-added spectrum in terms of flux as a function of the radial velocity of the [O III] $\lambda 5007$ line, with respect to the systemic velocity calculated from our redshift. The significantly separated [O III] $\lambda 5007$ peaks agree with those from the moderate-resolution ground-based spectra of Nelson & Whittle (1995), with the higher peak being at near systemic velocity ($v_r = -50 \text{ km s}^{-1}$) and the secondary red peak at $v_r = 800 \text{ km s}^{-1}$, meaning any [O III] emission not covered by the STIS long-slit observations does not significantly alter the profile shape or structure.

To determine the kinematics of the NLR, we incorporated the processed spectral images into a program that fits [O III] $\lambda 5007$ emission-line components with Gaussians over an average continuum, taken from available line-free regions in the spectra (Das et al. 2005). In order to get the maximum number of measured lines per data set, spectra were smoothed with a boxcar average using a width of 7 pixels. This smoothing allowed for the fitting of extended, low flux [O III] emission lines, without inhibiting us from deblending multiple [O III] lines dependent on different kinematic components along the slit. Calculating the central peak location for each Gaussian allowed us to determine the central wavelength for the corresponding [O III] line, which in turn was used to calculate its Doppler shifted velocity. There were three sources of uncertainty in our velocity measurements, as detailed by Das et al. (2005). The first is that the measured emission lines are not perfect Gaussians, the second comes from emission cloud displacements from the center of the $0''.2$ slit in the dispersion direction, and the third comes from noisy spectra. Errors were converted to velocities and added in quadrature, which produced a total maximum error of $\pm 60 \text{ km s}^{-1}$. Extremely noisy spectra (spectra without detectable emission $> 3\sigma$) at locations $\geq 3'' - 3''.5$ to the west and $\geq 3''.75$ ($4''.25$ for slit D) to the east of the nucleus, were not fitted. Subtracting the systemic velocity of the galaxy ($cz = 11037 \text{ km s}^{-1}$) from velocities calculated via [O III] line centroid shifts, we were able to determine the radial velocities along each slit in the rest frame of Mrk 78.

3. Results

Figures 3 and 4 show the rest frame radial velocities, FWHM, and normalized fluxes for the measured [O III] $\lambda 5007$ emission lines from the four slit positions. Kinematics from

the lower spectral resolution IR spectrum of Ramos Almeida et al. (2006) and the spectral images of Whittle et al. (2002) agree with our measurements. In general, the structure of the emitting region is clumpy in nature, as seen in the large number of flux peaks in each slit that can be matched to individual bright knots in the [O III] image of Figure 2. While each knot appears to have an individual peculiar velocity, the velocity field as a whole is relatively well organized. High radial velocities on both sides of the nucleus show the distinct asymmetrical red/blue shifts characteristic of biconical outflows seen in several other low-redshift Seyfert galaxies (Ruiz et al. 2001; Das et al. 2005, 2006; Crenshaw et al. 2010a; Fischer et al. 2010). Emission eastward of the optical peak is dominantly redshifted from systemic velocity (henceforth ‘red lobe’) while emission westward of the optical peak is dominantly blueshifted (henceforth ‘blue lobe’). Breaking down our simulated ground based spectrum of Figure 2 into the individual slits A, B, and C, we find that the redshifted velocity peak is primarily due to a specific high-flux knot, best sampled in slit B. Figure 1 contains a circle around the location of the redshifted knot and Figure 3 has a bracket in slit B, located over the high-flux region which depicts the knot.

4. Models

To generate kinematic models, we assume the ionizing radiation responsible for the NLR is biconical in nature, as it is the simplest geometric shape produced by a central obscuring torus. As with our previous kinematic models (Das et al. 2005, 2006; Crenshaw et al. 2010a; Fischer et al. 2010), we also initially assume that the bicone is hollow, where the separate NLR emission components represent opposite sides of the bicone. We employed our kinematics program from (Das et al. 2005), which allows us to recreate the observed radial velocities along a fixed slit position by altering various parameters of our model bicone outflow.¹ Our models include seven alterable parameters with initial values taken from the [O III] image in Figure 1 (deprojected height of bicone [z_{max}], outer half-opening angle [θ_{max}], and position angle) and the kinematics from Figures 3 and 4 (maximum velocity [v_{max}] and turnover radius [r_t]), leaving the inner half-opening angle (θ_{min}) and inclination of the bicone axis out of the plane of the sky to be alterable parameters free of restriction. We adopted our previous velocity law (Fischer et al. 2010), a linear increase starting with zero km s^{-1} at the nucleus

¹Previous studies of Mrk 78 have suggested that the NLR outflow is being radially accelerated via radio jets (Whittle & Wilson 2004; Whittle et al. 2005). While our model does not include any specific source of acceleration, instead simply simulating general outward acceleration, we do not detect considerable differences in the velocities or dispersions of emission-line knots near radio knots from others in the overall outflow noted in Whittle et al. (2002).

and subsequent linear decrease at r_t ending at zero km s^{-1} , because it is the simplest law that matches the observations.

The FOC [O III] image of Figure 1 shows that the NLR is not symmetric on either side of the nucleus. The redshifted, NE cone is less dispersed, more conical in nature, and features cleaner kinematics from which we can discern separate kinematic components due to outflow emission in the fore and back side of the cone. Conversely, the blueshifted, SW cone appears to have a larger opening angle, with flocculent, knotty emission and resulting intricate kinematics. Though using initial parameters solely from the NE cone was enticing, we found that the bicone did not envelop the entirety of the west lobe. Thus, we expanded the model bicone outer opening angle to envelop all NLR emission in the [O III] image in Figure 2. We chose $\theta_{max} = 30^\circ$ as our initial opening angle and used the kinematic components of the NE cone as the basis for the majority of our fitting. The initial inclination parameter relied on the kinematics seen in Figures 3 and 4, as either side was either mostly redshifted or blueshifted, and the imaging in Figure 1 as the extended biconical structure on either side of the nucleus would be less pronounced if we were to be looking into the bicone (Schmitt & Kinney 1996). With these guidelines, we determined an intermediate angle was most appropriate for a starting position. To find the most successful model, we altered parameters across all data sets while applying specific centroid offsets and position angles for each slit until a specific set of free parameters created an acceptable fit to all four data sets. Final values for all model parameters are provided in Table 3. Interestingly, the final opening angle and position angle are nearly identical to the apparent, initial parameters taken from Figure 1 ($\theta_{max} = 30^\circ$ and $P.A. = 70^\circ$ respectively). In comparison to our previous studies (Ruiz et al. 2001; Das et al. 2005, 2006; Fischer et al. 2010), Mrk 78 has an extremely large NLR as well as a narrower, thicker (greater difference between θ_{max} and θ_{min}) bicone than all other targets thus far.

Figure 5 displays a good qualitative fit between the model created by our final set of parameters and the data. The model matches fairly well to the east of the nucleus as kinematics for both sides of the eastern lobe are discernible in multiple slits. One discrepancy worth discussing is the lack of model data (shaded regions) mainly to the west of the nucleus in Slits B and C between $-0''.25$ to $0''.5$ and $-0''.5$ to $1''.5$ respectively. As our kinematics model creates a well defined geometrical model bicone with a sharp apex, incorporating slit positions that are transversely offset from the nucleus will generate models that lack data near the nucleus as the slit does not pass over the model bicone. This is due to the simplicity of our model as we assume that the bicone has a sharp apex, which is obviously not the case in this and other Seyferts (Antonucci 1993; Crenshaw et al. 2010b; Fischer et al. 2010). Thus, slits B and C lack modeled kinematics in these regions as the actual emission lies outside our model bicone geometry.

5. Discussion

The available evidence indicates that Mrk 78 is *not* a double AGN. Observing the variance in flux across the slit, we see many bumps and peaks that are due to large, bright knots of emission-line gas, each with their own peculiar velocity inside the general outflow pattern. It is one of these knots, a bright red-shifted cloud traveling at $\sim 800 \text{ km s}^{-1}$ inside of the ionizing bicone, that is the source of the offset radial velocity peak. The cloud appears to fit well in our modeled outflow pattern, supporting the suggestion by Crenshaw et al. (2010b) that uneven outflow can account for such dual-peaked profiles, and thus there is no need to assume there is a second AGN present. In comparison to our previous studies, kinematics for the NLR in Mrk 78 actually look rather similar to those in NGC 4151 (Hutchings et al. 1998; Crenshaw et al. 2000; Das et al. 2005), NGC 1068 (Crenshaw & Kraemer 2000; Das et al. 2006, 2007), Mrk 3 (Ruiz et al. 2001; Crenshaw et al. 2010a), and Mrk 573 (Schlesinger et al. 2009; Fischer et al. 2010). For each of these targets, including Mrk 78, we have successfully employed our biconical outflow models to find a good match to the overall flow patterns as a function of distance from the central AGN. Though there are some inconsistencies between the model and the data that are likely due to the simplified geometry of our bicone model and peculiar velocities of individual emission-line knots, radial outflow of [O III] clouds can explain the general, large-scale flow pattern of the NLR in Mrk 78, as well as the double peaked emission.

Does obscuration from dust contribute to the creation of the dual-peaked radial velocity profile as mentioned in Crenshaw et al. (2010b)? Ground based images of Mrk 78 in B and I give a position angle and inclination of the host galaxy as 84° and 64° respectively (Schmitt & Kinney 2000; Kinney et al. 2000). Adding this geometry to a geometric bicone model, we can test to see if a smooth distribution of dust contributed by the disk could be responsible for the radial velocity profile. Figures 6 and 7 show simple, three-dimensional geometric models of the ionizing bicone’s outer surface using θ_{max} , position angle, and inclination values from our final kinematics model and an additional two-dimensional galactic disk using the above position angle and inclination values. Though it is unknown which side of the disk is closer, either geometry in combination with our final bicone model results in a radial velocity profile that is either symmetric or asymmetric towards the blue. The latter case can be seen in Figure 6 as the redshifted cone should be more extinguished by dust in the galactic plane. This scenario does not fit our data as the blue-shifted, likely less obscured lobe would then contribute a majority of the total emission-line flux. Thus, it is unlikely that a dusty disk would be responsible for the given profile.

There is a prominent dust lane that sweeps over the center of the AGN. Each image in Figure 1 shows a distinct band from southeast to northwest across the nucleus with a

position angle of $\sim 123^\circ$ southeast to northwest that has flux much lower than the emission surrounding it. More quantitatively, we obtained an additional STIS G750M (5450 - 10140Å) spectrum from MAST taken along the same position as the G430M slit D in order to measure the flux ratio of $H\alpha/H\beta$ over the nucleus, and calculated a reddening of $E(B - V) = 0.78$ (assuming a galactic reddening curve and intrinsic $H\alpha/H\beta = 2.9$). The reddening is significant enough to extinguish portions of the inner NLR, possibly suppressing high-velocity dispersion emission from the bicone at $\sim 0 \text{ km s}^{-1}$ and making the double line profile more distinct. However, this reddening is not enough to extinguish the AGN broad-line region (BLR). As such, it is likely that this dust lane must be additional obscuration external to the "torus".

Further evidence for a dust lane can be seen in the blue-shifted southwest lobe from the imaging shown in Figure 1. From the end of the absorbing dust lane, an arc of emission is visible along the north rim of the lobe $\sim 2''$ from the "+" marking the continuum peak location. It remains unclear whether the dust lane crossing across the nucleus arcs over the southwest lobe and continues to absorb emission or instead arcs into the ionizing bicone and becomes illuminated, similar to Mrk 3 and Mrk 573 (Crenshaw et al. 2010a; Fischer et al. 2010). However, both situations would help explain the asymmetrical, patchy emission seen in the blue-shifted emission lobe. Figure 6 depicts a galactic disk with the north side of the disk coming out of the page, which allows for a potential interaction between the disk and ionizing bicone. A full understanding of this extended morphology will require more thorough imaging before a more accurate claim can be made.

6. Conclusions

We have analyzed STIS long-slit G430M spectra of the inner emission knots and nucleus of the Seyfert 2 galaxy Mrk 78. We generated kinematic and geometrical models of the NLR and ENLR that successfully fit the data, with the final parameters of Mrk 78's outflow bicone given in Table 3. While it is not clear at this time how the blue-shifted lobe is interacting with the dust lane lying over the nucleus, it is likely that that interaction can explain the dispersed morphology present in the given FOC and STIS imaging.

We find that the double peaked emission lines seen in ground-based spectra of Mrk 78 are due to an asymmetric distribution of outflowing gas in the NLR. Specifically, the red peak at $+800 \text{ km s}^{-1}$ is due to a bright emission-line knot that is redshifted with respect to the systemic velocity of the host galaxy. The bright, redshifted knot follows the same flow pattern as the other knots, and thus, there is no need to assume that a second AGN resides within Mrk 78. Furthermore, all Seyferts that we have modeled to date show

outflows (Ruiz et al. 2001; Das et al. 2005, 2006; Fischer et al. 2010), and thus asymmetric distributions of outflowing gas and/or patchy dust extinction maybe a general explanation for double-peaked emission-line profiles. With nothing unusual separating Mrk 78 from other AGN, it is possible that many double-peaked profiles may be due to outflows in a single AGN as shown by our models.

Table 1. *HST*/STIS G430M Observations of Mrk 78

| Slit | Exposure (s) | P.A. (degrees) | Offset ^a (arcsec) |
|------|-----------------|-------------------|---------------------------------|
| A | 1727 | 88 | 0.125 |
| B | 1938 | 88 | -0.27 |
| C | 2052 | 88 | -0.55 |
| D | 1800 | 61 | -0.05 |

^aCross-dispersion offset from the optical continuum peak. A positive value corresponds to a displacement south of the slit P.A. axis in Figure 1.

Table 2. *HST*/FOC/STIS Imaging Observations of Mrk 78

| Instrument | Filter | Exposure (s) |
|------------|--------|-----------------|
| STIS | MIRVIS | 120. |
| FOC | 372M | 896. |
| FOC | 550M | 1196. |
| FOC | 502M | 801. |

Table 3. Best Fit Model Parameters for Mrk 78^a

| Parameter | Values |
|----------------|--------------------------|
| $P.A.$ | 65° |
| i | $30^\circ(\text{SW})$ |
| θ_{max} | 35° |
| θ_{min} | 10° |
| v_{max} | 1200 km s^{-1} |
| z_{max} | 3200 pc |
| r_t | 700 pc |

^aThe letters in parentheses indicates the side closest to us.

REFERENCES

- Adams, T. F. 1973, *ApJ*, 179, 417
- Antonucci, R. 1993, *ARA&A*, 31, 473
- Arribas, S., Mediavilla, E., & Garcia-Lorenzo, B. 1996, *ApJ*, 463, 509
- Christopoulou, P. E., Holloway, A. J., Steffen, W., Mundell, C. G., Thean, A. H. C., Goudis, C. D., Meaburn, J., & Pedlar, A. 1997, *MNRAS*, 284, 385
- Comerford, J. M. et al. 2009, *ApJ*, 698, 956
- Crenshaw, D. M., & Kraemer, S. B. 2000, *ApJ*, 532, L101
- Crenshaw, D. M. et al. 2000, *AJ*, 120, 1731
- Crenshaw, D. M., Kraemer, S. B., Schmitt, H. R., Jaffé, Y. L., Deo, R. P., Collins, N. R., & Fischer, T. C. 2010a, *AJ*, 139, 871
- Crenshaw, D. M., Schmitt, H. R., Kraemer, S. B., Mushotzky, R. F., & Dunn, J. P. 2010b, *ApJ*, 708, 419
- Dahari, O., & De Robertis, M. M. 1988, *ApJ*, 331, 727
- Das, V. et al. 2005, *AJ*, 130, 945
- Das, V., Crenshaw, D. M., & Kraemer, S. B. 2007, *ApJ*, 656, 699
- Das, V., Crenshaw, D. M., Kraemer, S. B., & Deo, R. P. 2006, *AJ*, 132, 620
- De Robertis, M. M., & Shaw, R. A. 1990, *ApJ*, 348, 421
- Elitzur, M., & Shlosman, I. 2006, *ApJ*, 648, L101
- Fischer, T. C., Crenshaw, D. M., Kraemer, S. B., Schmitt, H. R., & Trippe, M. L. 2010, *AJ*, 140, 577
- Hutchings, J. B. et al. 1998, *ApJ*, 492, L115+
- Kinney, A. L., Schmitt, H. R., Clarke, C. J., Pringle, J. E., Ulvestad, J. S., & Antonucci, R. R. J. 2000, *ApJ*, 537, 152
- Komossa, S. et al. 2008, *ApJ*, 678, L13
- Liu, X., Greene, J. E., Shen, Y., & Strauss, M. A. 2010, *ApJ*, 715, L30

- Nelson, C. H., & Whittle, M. 1995, *ApJS*, 99, 67
- Pogge, R. W. 1988, *ApJ*, 328, 519
- Ramos Almeida, C., Pérez García, A. M., Acosta-Pulido, J. A., Rodríguez Espinosa, J. M., Barrena, R., & Manchado, A. 2006, *ApJ*, 645, 148
- Rodríguez-Ardila, A., Prieto, M. A., Viegas, S., & Gruenwald, R. 2006, *ApJ*, 653, 1098
- Ruiz, J. R., Crenshaw, D. M., Kraemer, S. B., Bower, G. A., Gull, T. R., Hutchings, J. B., Kaiser, M. E., & Weistrop, D. 2001, *AJ*, 122, 2961
- Sargent, W. L. W. 1972, *ApJ*, 173, 7
- Schlesinger, K., Pogge, R. W., Martini, P., Shields, J. C., & Fields, D. 2009, *ApJ*, 699, 857
- Schmitt, H. R., Donley, J. L., Antonucci, R. R. J., Hutchings, J. B., & Kinney, A. L. 2003, *ApJS*, 148, 327
- Schmitt, H. R., & Kinney, A. L. 1996, *ApJ*, 463, 498
- . 2000, *ApJS*, 128, 479
- Schmitt, H. R., Storchi-Bergmann, T., & Baldwin, J. A. 1994, *ApJ*, 423, 237
- Storchi-Bergmann, T., Wilson, A. S., & Baldwin, J. A. 1992, *ApJ*, 396, 45
- Vrtilek, J. M., & Carleton, N. P. 1985, *ApJ*, 294, 106
- Whittle, M. 1985, *MNRAS*, 213, 1
- Whittle, M., Pedlar, A., Meurs, E. J. A., Unger, S. W., Axon, D. J., & Ward, M. J. 1988, *ApJ*, 326, 125
- Whittle, M., Rosario, D. J., Silverman, J. D., Nelson, C. H., & Wilson, A. S. 2005, *AJ*, 129, 104
- Whittle, M., & Wilson, A. S. 2004, *AJ*, 127, 606
- Whittle, M., Wilson, A. S., Nelson, C. H., Rosario, D., & Silverman, J. D. 2002, in *Revista Mexicana de Astronomía y Astrofísica*, vol. 27, Vol. 13, *Revista Mexicana de Astronomía y Astrofísica Conference Series*, ed. W. J. Henney, W. Steffen, L. Binette, & A. Raga, 230–235

Fig. 1.— Composite of *HST* STIS acquisition continuum image (left) with additional enlarged [O III] (F502M filter, as seen in Schmitt & Kinney (1996)) and UV (F372M filter, mainly [OII] emission) FOC images (middle and right respectively). The dust lane sweeping over the AGN is located at a position angle of $\sim 123^\circ$ southeast to northwest. STIS slit positions have been superimposed and the red-shifted emission knot responsible for the secondary radial velocity peak is circled on the [O III] image.

Fig. 2.— Summation of spectral flux from slits A, B, and C as a function of radial velocity for the [O III] $\lambda 5007$ emission line with respect to the systemic velocity. Double peaked [O III] $\lambda 4959$ emission-line profile is seen to the left.

Fig. 3.— Radial velocities (top), FWHM (middle), and normalized total flux (bottom) of [O III] measurements for slits A and B. The bracket in slit B shows the location of the high flux cloud responsible for the secondary radial velocity peak.

Fig. 4.— Radial velocities (top), FWHM (middle), and normalized total flux (bottom) of [O III] measurements for slits C and D.

Fig. 5.— Shaded regions represent the kinematic model chosen as the best fit for our radial velocity data set for all four slits. Parameters used to create this model are given in Table 1. Lighter regions represent kinematics for the side of each cone near parallel to our line of sight, darker regions represent kinematics for the side near perpendicular to our line of sight.

Fig. 6.— Geometric model of the NLR based on parameters from Table 1, shown as viewed from Earth. Inner disk geometry is taken from Kinney et al. (2000) depicting the top of the disk coming out of the sky. The yellow bar represents the position angle of the dust lane traveling over the nucleus. The bright redshifted knot is in the northeast portion of the bicone.

Fig. 7.— Same as Figure 6, except the inner disk geometry depicts the bottom of the disk coming out of the sky. The yellow bar represents the position angle of the dust lane traveling over the nucleus.

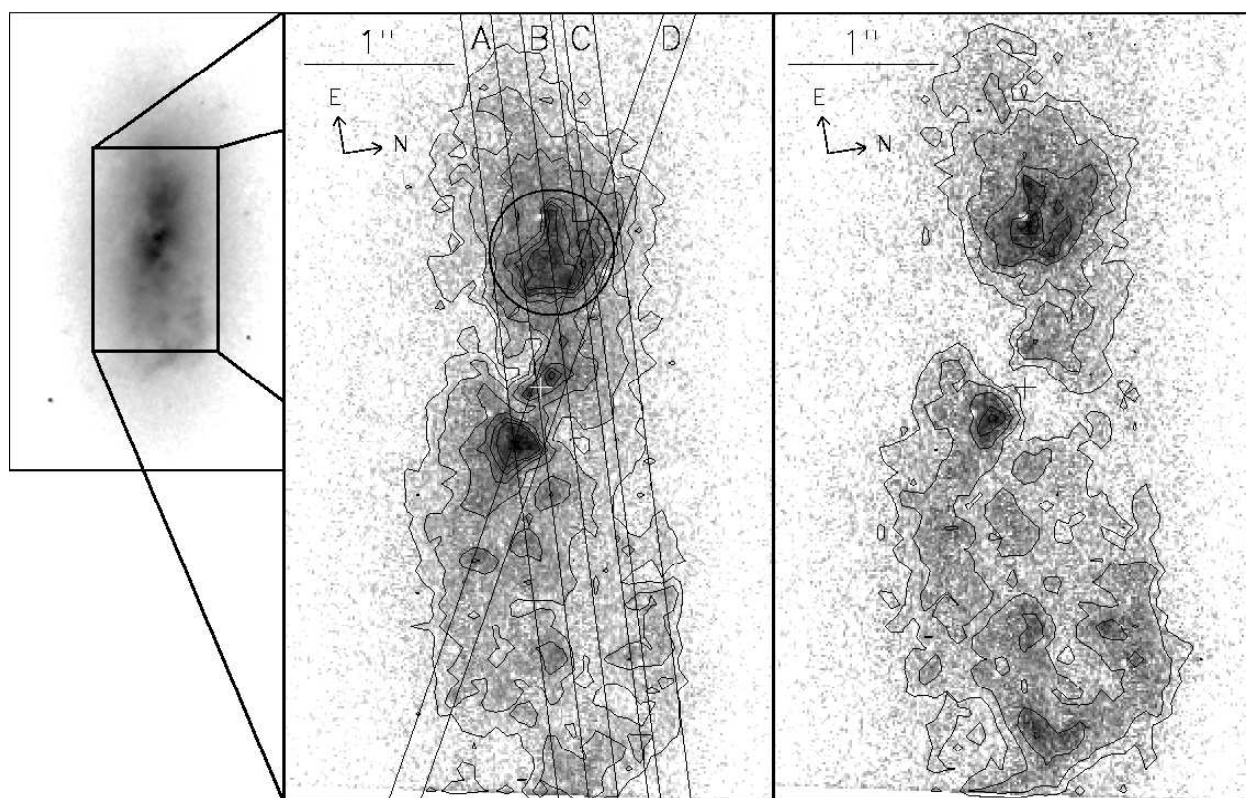


Fig. 1.

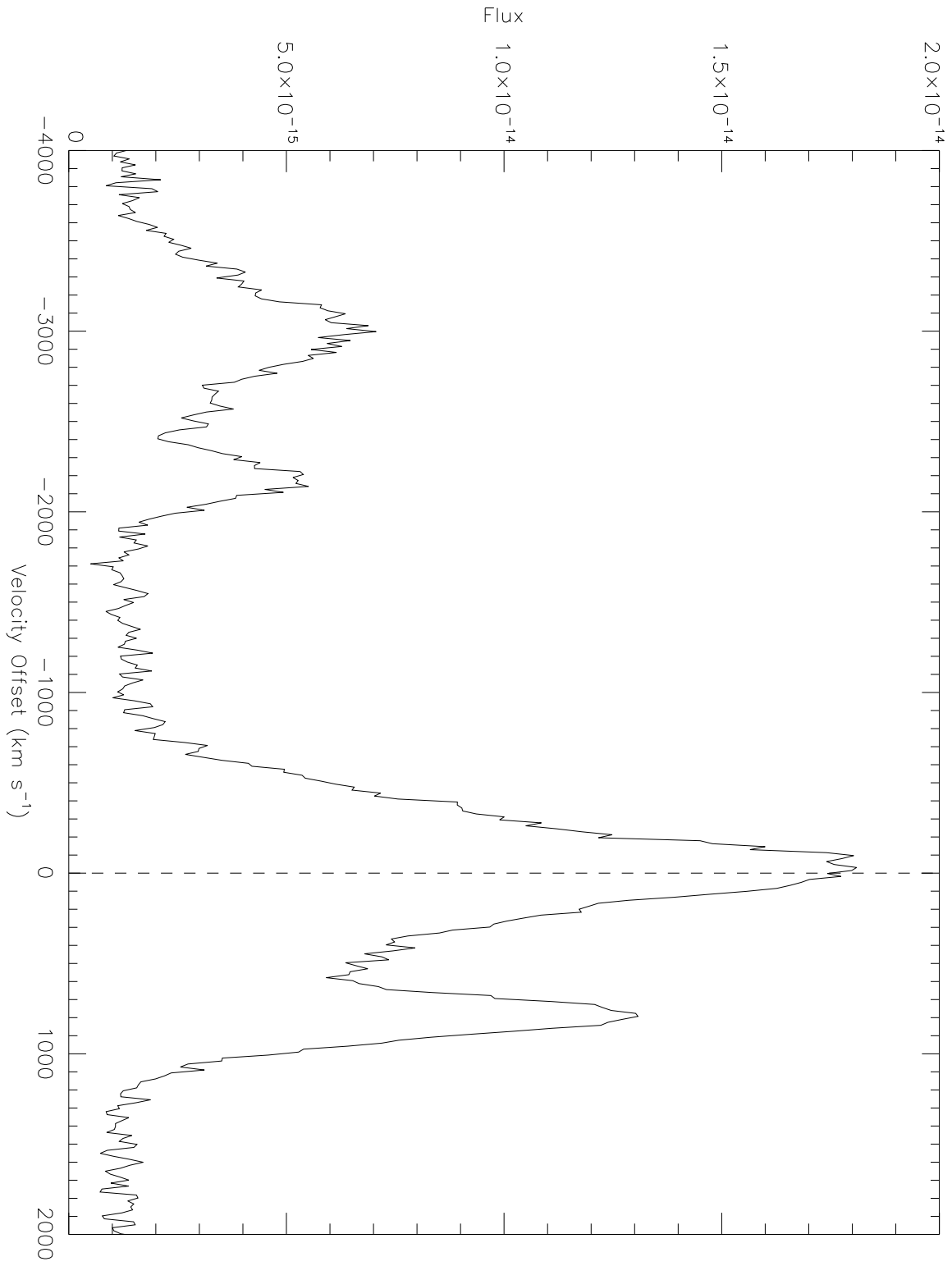


Fig. 2.

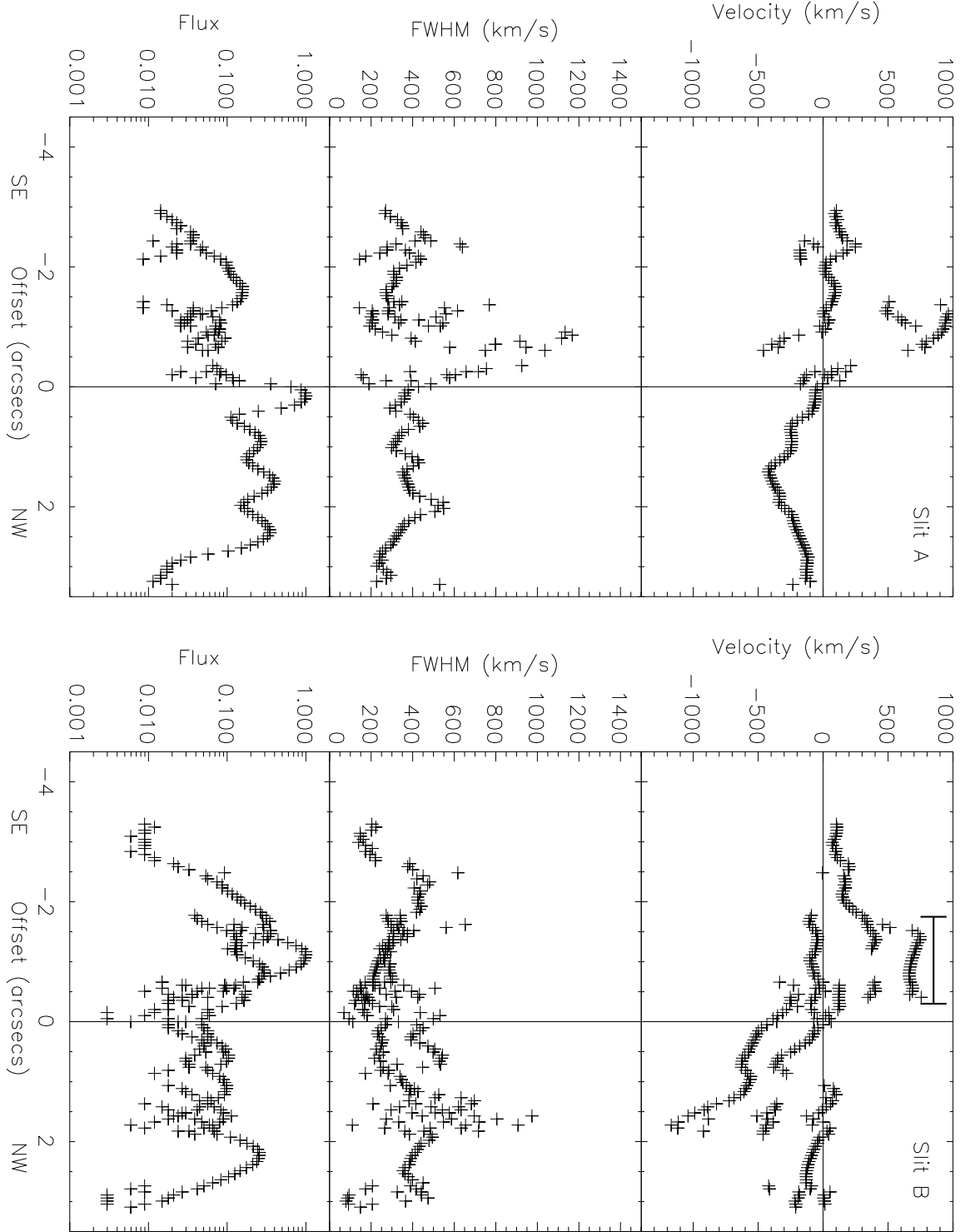


Fig. 3.

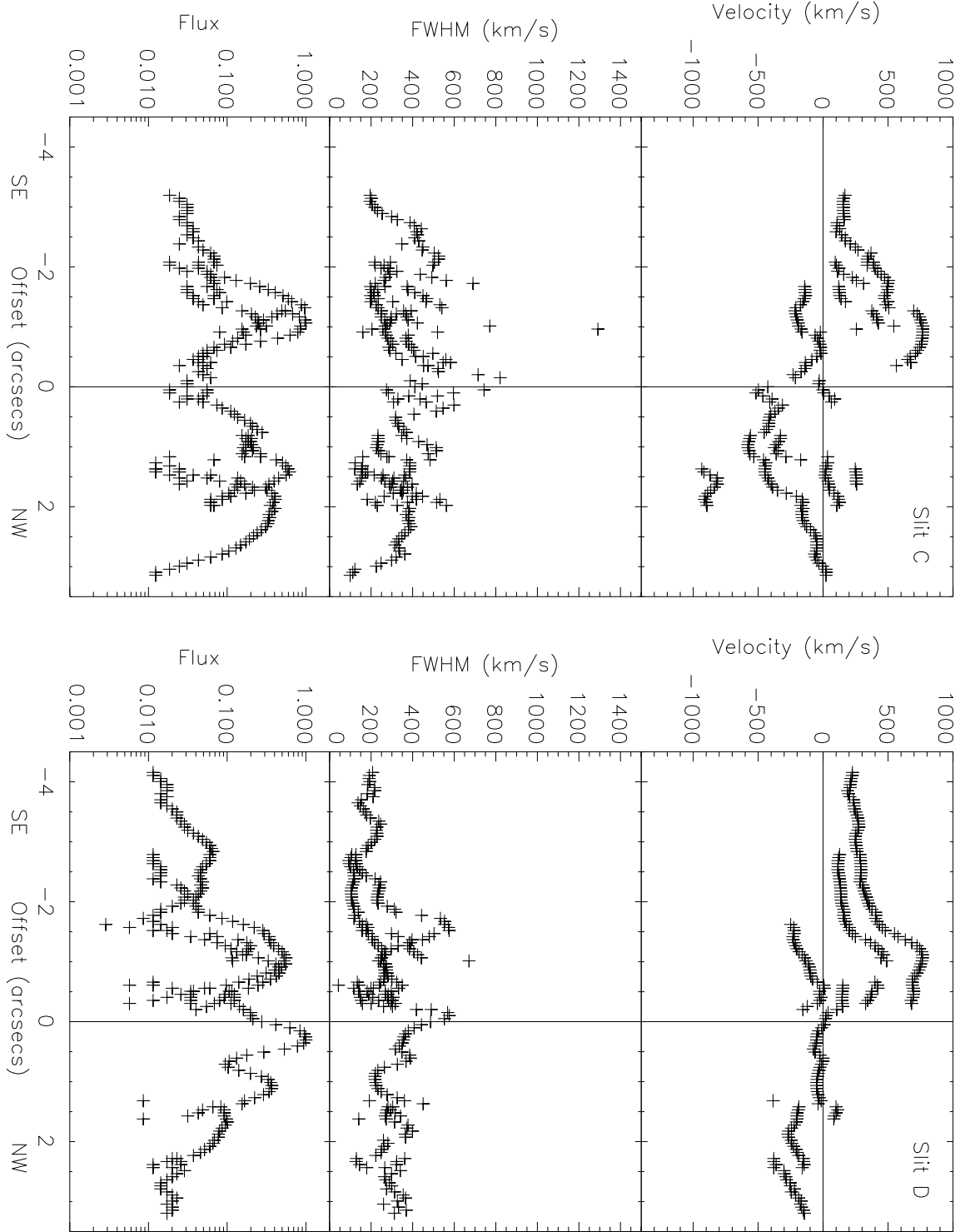


Fig. 4.

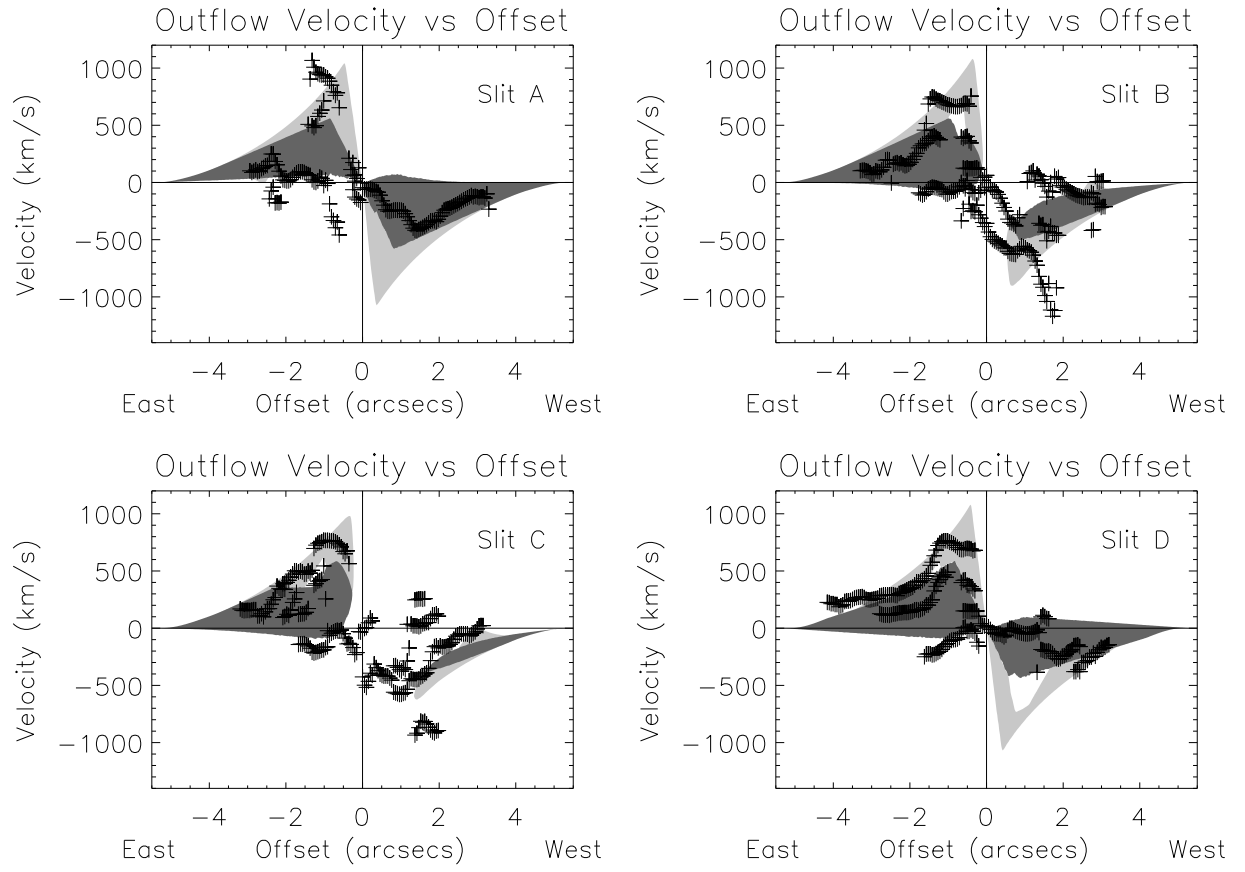


Fig. 5.

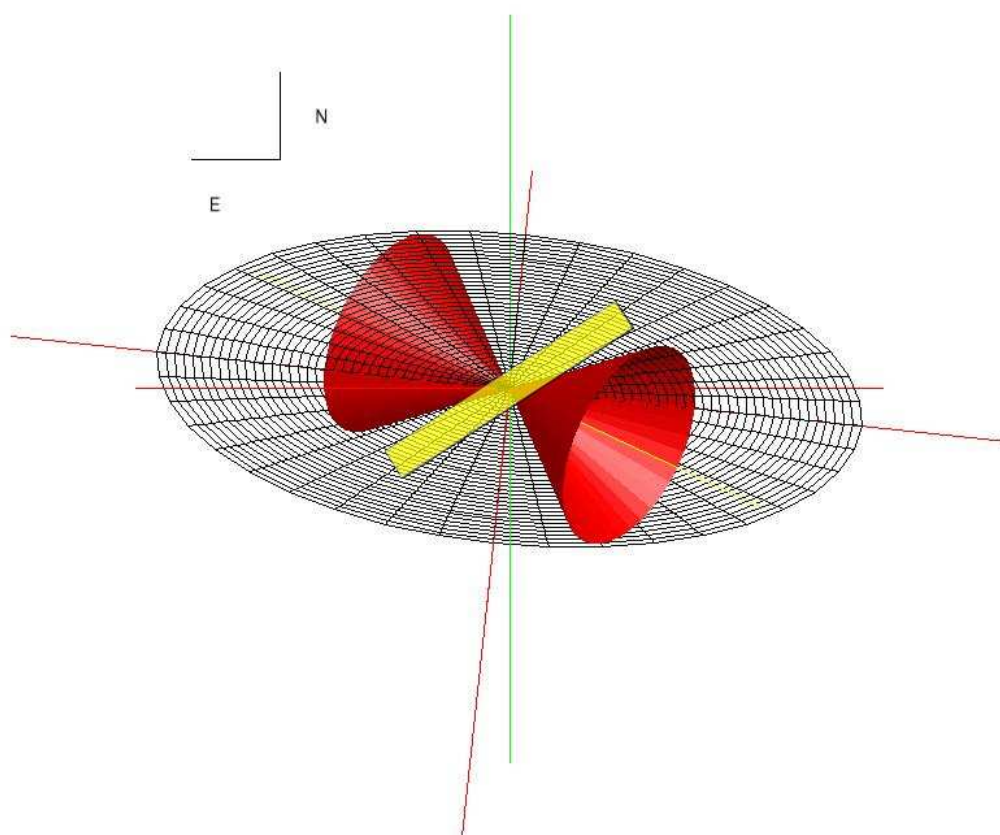


Fig. 6.

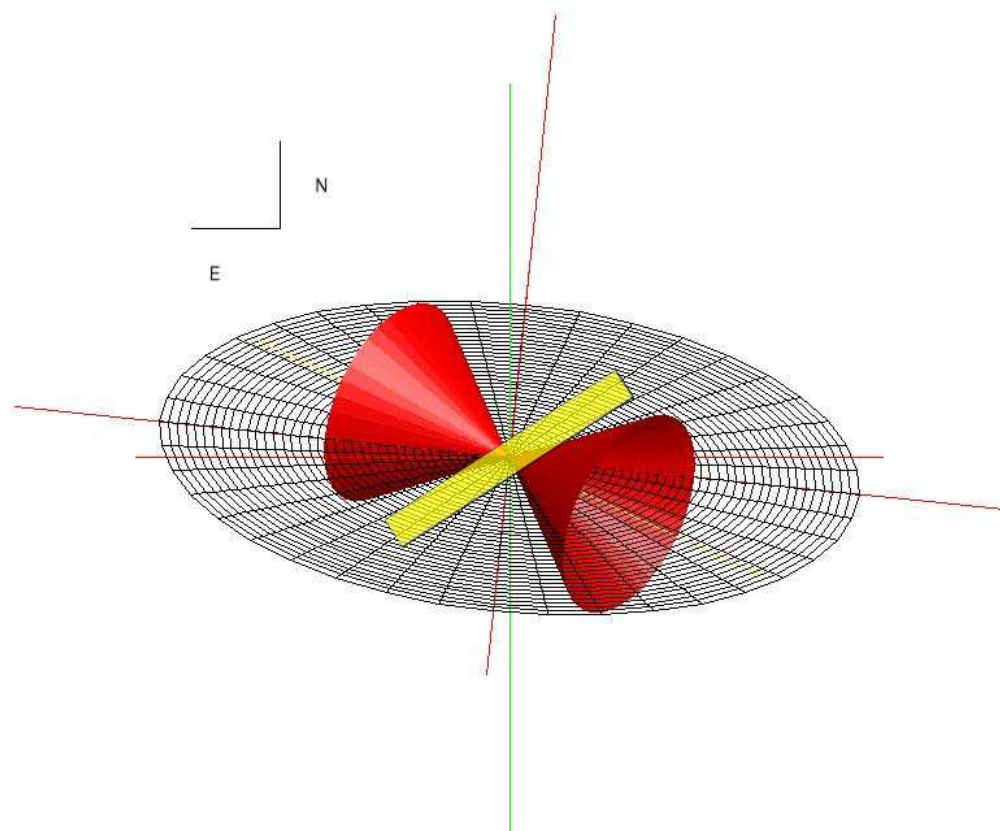


Fig. 7.